# Increasing the Aerodynamic Performance of a Formula Student Race Car by Means of Active Flow Control

**5 authors**, including:

Ben Steinfurth
Technische Universität Berlin
**7** PUBLICATIONS   **0** CITATIONS

SEE PROFILE

Arne Berthold
Technische Universität Berlin
**9** PUBLICATIONS   **3** CITATIONS

SEE PROFILE

Steffen Feldhus
Technische Universität Berlin
**3** PUBLICATIONS   **0** CITATIONS

SEE PROFILE

Frank Haucke
Technische Universität Berlin
**29** PUBLICATIONS   **124** CITATIONS

SEE PROFILE

Some of the authors of this publication are also working on these related projects:

Impingement cooling by pulsating jet-arrays View project

blended wing body View project

# Increasing the Aerodynamic Performance of a Formula Student Race Car by Means of Active Flow Control

B. Steinfurth, A. Berthold, S. Feldhus, F. Haucke, J. Weiss

## Abstract

This article involves an experimental study regarding the capability of fluidic actuators to increase the aerodynamic performance of a four-element race car rear wing. Sweeping jet actuators are integrated in the upper flap, of which the angle of attack is increased by up to $\Delta\alpha_{F3} = 40°$ with reference to a passively optimized setup. Different velocities of the emitted sweeping jets are applied to study the influence of momentum coefficients $c_\mu = 0.04 ... 0.98$ %. To prove the feasibility of the approach, flow control is first applied to a stand-alone rear wing tested in a small wind tunnel. Subsequently, a realistic race car model featuring the controlled rear wing is investigated in a larger-scale wind tunnel. Employing particle image velocimetry, flow visualization techniques as well as pressure and force measurements, we show that the velocity field on the suction side of the upper flap is characterized by flow separation of different degrees when the angle of attack is increased beyond $\Delta\alpha_{F3} = 20°$ (rear wing only) and $\Delta\alpha_{F3} = 30°$ (complete race car). Generally, the employed fluidic devices have a positive impact in terms of the aerodynamic performance for all investigated angles of attack as overall downforce increases by up to 22 % are achieved, however accompanied by larger drag. Nonetheless, an in-house simulation indicates a potential lap time reduction of 0.17 % at the Formula Student endurance race circuit at Hockenheim under permanent actuation. Even greater gains are to be expected for a selective employment during cornering only or for skidpad and acceleration competitions.

## Introduction

Along with other contributing factors, a sophisticated aerodynamic design is essential in maximizing the performance of a race car. The significance of this measure is obvious in view of the fact that a 1% increase in aerodynamic downforce (negative lift) yields a lap time reduction of 0.1 seconds at Silverstone Grand Prix Circuit [1]. The enhanced traction, typically required for acceleration phases and cornering maneuvers where high inertial forces in lateral direction occur, is majorly generated by employing aerodynamic devices, such as front, rear and side wings. With these devices downforce that can be more than two times the weight force of the race car is generated [2].

Effectively increasing the camber of a wing, multi-element configurations consisting of one main wing and one or more slotted flaps are frequently utilized on race cars [3]. In these arrangements, generally associated with high-lift aerodynamics, the gap flow of air from the pressure side of one wing is not only rendering flow separation on the downstream flap less likely but also increasing the velocity on the suction side of the primary element. Compared to non-slotted flaps, the angle of attack can thus be further increased, yielding a proportional enhancement in the generated force. However, this relation only holds true as long as the flow remains attached. When the angle of attack is too high, the induced adverse pressure gradient causes flow separation, which is accompanied by a performance drop.

An established countermeasure consists in the emission of compressed air close to the separation point. Thus, the kinetic energy of the boundary layer is raised, rendering it less likely to separate from the surface for otherwise overcritical operating conditions. While steady jets were successfully employed in the context of active separation control (ASC) initially, unsteady blowing has been established as the more effective and efficient approach in the last decades [4]. Successful suppression or delay of boundary layer separation on multi-element wings has been achieved with various approaches, e.g., valve controlled pulsed jet actuators (PJAs) [5,6], synthetic jets [7] and plasma actuators [8]. Despite the great number of demonstrations of their capability, these mechanically or electrically driven devices are rarely used in industrial applications. This is partly due to the integration cost, the need for an electrical supply system and maintenance charges that often cannot be offset by the aerodynamic benefit from an economic perspective.

Fluidic devices on the other hand generate unsteady jets owing to internal flow mechanisms. They are robust due to a lack of moving parts, easy to fabricate and do not require a power supply. Along with fluidic PJAs [9], sweeping jet actuators (SJAs) are a prominent member of this category. They produce spatially oscillating jets with their momentum input distributed over a flow region that is large compared to the dimensions of the device [10], having a mass flow dependent sweeping frequency [11]. When interacting with a crossflow, the sweeping jet produces a pair of counter-rotating vortices that prevail far downstream of the SJA outlet [12]. Furthermore, the trajectories of these longitudinal structures are shallower compared to steady jets, enabling an efficient transfer of high-momentum fluid toward the wall. This makes them particularly attractive for ASC applications where several promising investigations have been conducted. For example, flow separation was effectively suppressed on the rudder of a vertical tail, increasing the generated side force by up to 50 % for sub- and 20 % for full-scale tests respectively [13,14]. SJAs were also successfully applied on the flap shoulder of a two-element high-lift configuration [15]. In the field of road vehicle aerodynamics, they were used on the c-

pillars and the roof/rear window junction of the *DrivAer* model and on the base of a generic truck model to produce drag reductions by 3.5 % and 7 % respectively [16,17]. Furthermore, a favorable scalability of the approach was attested considering the simplified Ahmed body [18].

In terms of the actuation parameters, neither the mass flow rate nor the momentum input appears to be the sole quantity governing the control authority, but both need to be considered adequately. It is also interesting to note that the optimal outlet location is not dependent on angle of attack, actuation intensity or flap deflection for a generic airfoil [19]. A further parameter study suggests that this location needs to be close to the mean separation point and a wide spreading angle is to be favored for optimal performance [20].

Although ASC can generally be considered an established means to improve the efficiency of various applications, to the best of our knowledge, it has not been employed to enhance the aerodynamic performance of a race car. The aim of this study is to close this research gap and determine the aerodynamic effects of SJAs applied on the four-element rear wing of a realistic open-wheel race car model whose main properties are well known from a previous investigation [21]. For this purpose, flow visualizations, force and pressure measurements were performed for different actuation intensities while the angle of attack of the third flap was varied. Additionally, the flow field inside relevant areas on the wing was measured by performing stereoscopic particle image velocimetry (PIV). Based on the obtained results, we estimate potential lap time reductions and propose methods to implement the approach on a full-scale race car.

## Experimental Setup

In the following, information regarding the measurement setup and procedure for the preliminary and main experiments carried out in this study are provided with a focus on the investigated rear wing and the employed measurement techniques.

### *Four-Element Rear Wing*

The four-element wing investigated in this study is shown in Figure 1. It is an aerodynamic component of the *FT18* model of *FaSTTUBe – Formula Student Team TU Berlin*.
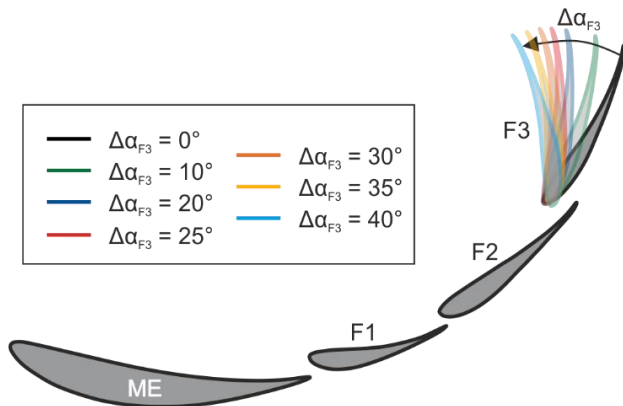


Figure 1. Investigated race car rear wing and illustration of angle of attack variation of upper flap

The team regularly takes part in international Formula Student events where restrictions regarding the dimensions of the installed rear wings are imposed, as it is bounded by the inner sides of the rear wheels and the head restraint and must not exceed the wheels in streamwise direction by more than 250 mm. Furthermore, it must not exceed a mounting height greater than 1200 mm.

In this study, a 3D printed 1:3 scale model of the rear wing is investigated with the general geometrical parameters stated in Table 1.

Table 1. Geometrical specifications of rear wing elements for this study; angle of attack with reference to the horizontal.

| Rear wing element | Chord length [mm] | Angle of attack [°] |
|---|---|---|
| Main element (ME) | 113.6 | -5.9 |
| First flap (F1) | 53.3 | 13.7 |
| Second flap (F2) | 66.7 | 39.2 |
| Third flap (F3) | 66.7 | 63.3 + [10 ... 40] |

Due to the mentioned restrictions limiting the maximum size of the rear wing, a time-consuming design process is an effort worth taking to provide optimum aerodynamic characteristics. For this purpose, the geometrical setup of the wing elements is optimized numerically before simulations of the entire race car are conducted. As displayed in Figure 2, the wake of this race car is very complex and may exhibit flow separation on the midsection of the upper rear wing flap for certain angles of attack as indicated by the swirling strength, i.e., the imaginary part of the complex eigenvalues of the velocity gradient tensor. This results in a decreased downforce und thus, limits the range of operable angles of attack.
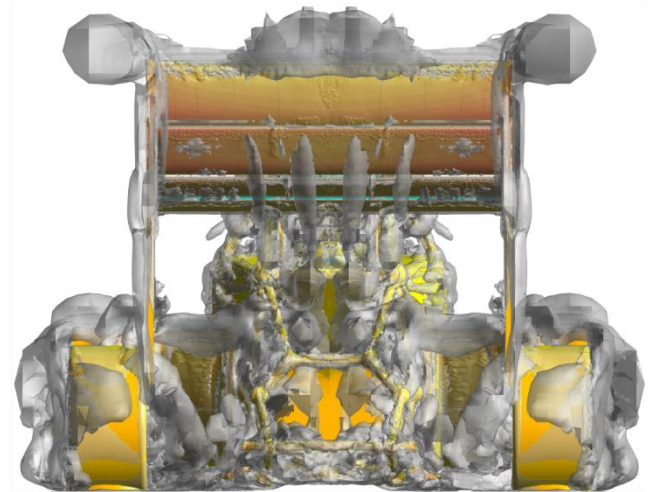


Figure 2. Rear view of *FT18* race car; grey iso-contours indicate vortex structures associated with flow separation.

To counter any pressure-induced separation in the present experimental study, 26 SJAs were integrated inside the F3 element with an outlet width of $d \approx 1.3$ mm and a spanwise spacing of $s \approx 8.6\, d$. The outlets were located at 25% chord as a compromise between expected aerodynamic benefit and integrability of the devices. The emission angle with respect to the surface tangent was $\varphi = 30°$. To provide this angle, the actuator geometry was slightly curved as depicted in Figure 3.

## 3D printed parts prior to mating
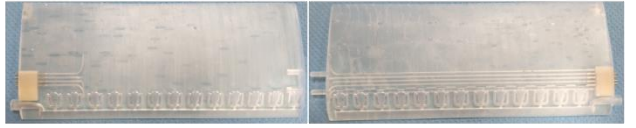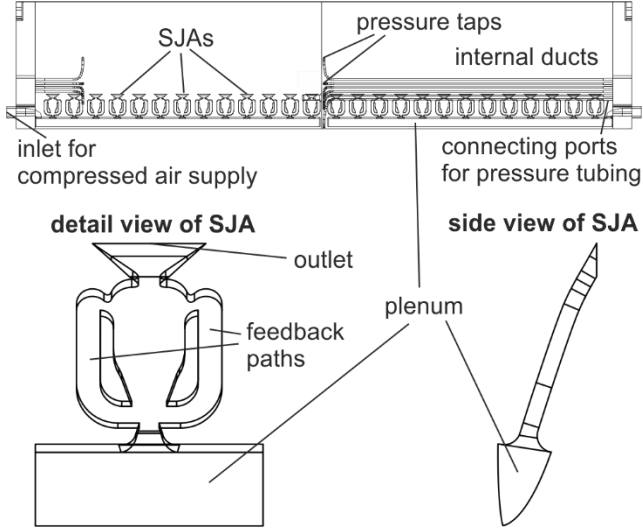


## suction side of upper flap F3



*Figure 3. Upper flap F3 with 26 SJAs and internal actuator geometry.*

After entering the device through a plenum, the air is deflected to one side of the internal interaction chamber where a small part is fed into the respective feedback path before deflecting the incoming flow towards the other side of the device. This process proceeds in a periodic manner, producing a sweeping jet emitted through the outlet. For further details regarding the internal mechanisms, the reader is referred to [22].

The almost linear dependence of the frequency on the jet velocity for the employed SJA is shown in Figure 4. Note that the jet velocity is estimated on the basis of the control mass flow via mass conservation.
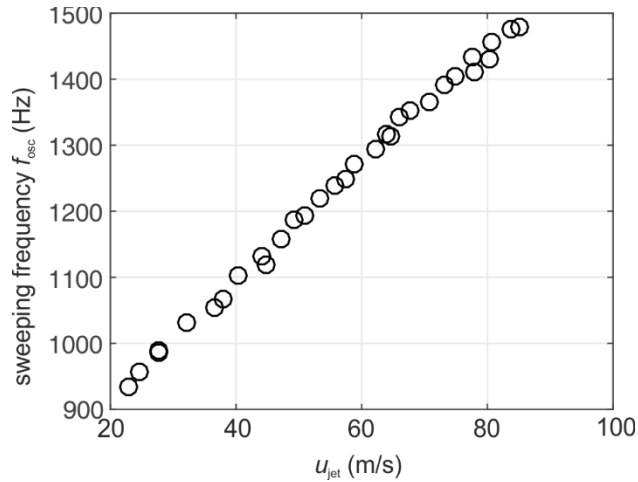


*Figure 4. Sweeping frequency of the SJA as a function of jet velocity.*

## Experimental Setup and Measurement Procedure

This study involves a preliminary investigation of the stand-alone rear wing to verify the general feasibility of the ASC approach. In a second step, the influence on the aerodynamic characteristics of the complete race car is studied in a large-scale wind tunnel.

The preliminary experiments were conducted using an open subsonic *Eiffel* type wind tunnel with a maximum velocity of $U_\infty = 40$ m/s and a turbulence intensity of $Tu \approx 0.6\%$ at the $(0.4\ x\ 0.4)\ m^2$ nozzle outlet. The free stream velocity was $U_\infty = 20$ m/s for all cases, corresponding to a Reynolds number of $Re = 400.000$ based on the rear wing chord. Reynolds number independence is achieved at $Re > 360.000$ for the rear wing model.

For the main measurement campaign, the same 1:3 scale model of the FT17 model as in [21] was investigated. However, the rear wing of the FT18 was installed to identify its influence on the aerodynamic performance. The experiments were performed in a closed-loop subsonic wind tunnel at the same free stream velocity as the preliminary experiments, i.e., $U_\infty = 20$ m/s. Reynolds number independency in terms of lift and drag were verified. The maximum turbulence intensity was of the order of $Tu \approx 0.5$ % at the inlet of the test section (Figure 5) which had a cross section of $A = (2.00 \cdot 1.41)$ m$^2$, resulting in a blockage ratio of $\varphi \approx 4.7$ % in zero-yaw condition. No correction was applied since this value does not exceed the critical threshold stated in [23]. The model was mounted on a 6-component balance with an accuracy of 0.1 % of measured values, which allowed also for rotary movement to simulate crosswind conditions. Being relevant for cornering in most Formula Student events, yaw angles of $\beta = -21 \ldots 21°$ were investigated. A photo of the model inside the test section is supplied in the appendix of this article.
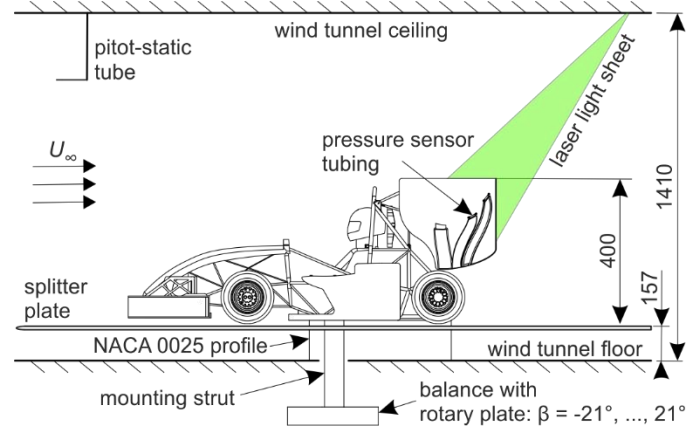


*Figure 5. Experimental setup for investigation of entire race car; based on depiction in [21].*

During the course of the preliminary measurements, the angle of attack of the upper flap F3 was increased by $\Delta\alpha_{F3} = [10, 20, 25]°$ with reference to a passively optimized angle of attack (Figure 1, Table 1). As flow separation only set in at even greater angles of attack when investigating the entire vehicle, increases up to $\Delta\alpha_{F3} = 40°$ were studied during the main measurement campaign.

To suppress any occurring flow separation, the impact of different velocity ratios $r = u_{jet}/U_\infty = [1,2,3,4,5]$ was studied, corresponding to momentum coefficients

$$c_\mu = \frac{\varrho_{\text{jet}}\, u_{\text{jet}}^2\, d}{1/2\, \varrho_\infty\, U_\infty^2\, c_{F3}} = [0.04, 0.16, 0.35, 0.62, 0.97]\,\%,$$

where $\varrho$ is the mass density of the supplied compressed air and the free stream respectively. As the sweeping frequency is dependent on the jet velocity, the applied variation in actuation intensity is associated with different frequencies $f_{\text{osc}} \approx$ $[900, 1100, 1300, 1450, 1600]$ Hz, corresponding to reduced frequencies of the order of

$$F^+ = (f_{osc}\, c_{F3})/u_{jet} \approx [3, 1.8, 1.4, 1.2, 1.1].$$

To visualize the onset of flow separation under variation of the angle of attack, UV active tufts were attached to the rear wing suction side. Long-time exposure images were taken using a single-lens reflex camera from a location sufficiently far downstream of the wing as to not affect the flow field.

Furthermore, Stereo-PIV was performed to measure the three velocity components inside the symmetry plane of the wing. In order to gain information regarding the entire flow field around the rear wing during the preliminary experiments, the velocity distributions in multiple planes shown in Figure 6 were measured individually before merging the time-averaged velocity fields that were based on 500 snapshots taken with a constant acquisition rate of 5 Hz. When investigating the entire model, only the velocity field on the upper flap suction side was measured with PIV.

For both experiments, the equipment consisted of a dual pulsed Nd:YAG laser and two cameras with an optical resolution of $(2560 \times 2160)\text{px}^2$; the spatial resolution of the obtained velocity data was $\Delta x = \Delta y < 1$ mm. Multiple FFT correlation and grid refinement were employed, resulting in a ratio of plausible data consistently greater than 95 %.

In addition, pressure measurements were conducted by means of piezo-resistive differential transducers with a range of $\Delta p_{max} = \pm[2000, 5000]$ Pa that were employed respecting the expected pressure magnitude. The positions of the 18 pressure taps from which the distributions of pressure coefficients were deduced on the three flaps, are shown in Figure 6. Note that hollow ducts were provided in the 3D printed wing elements in order to connect the pressure taps with the tubing mounted at the end plates.
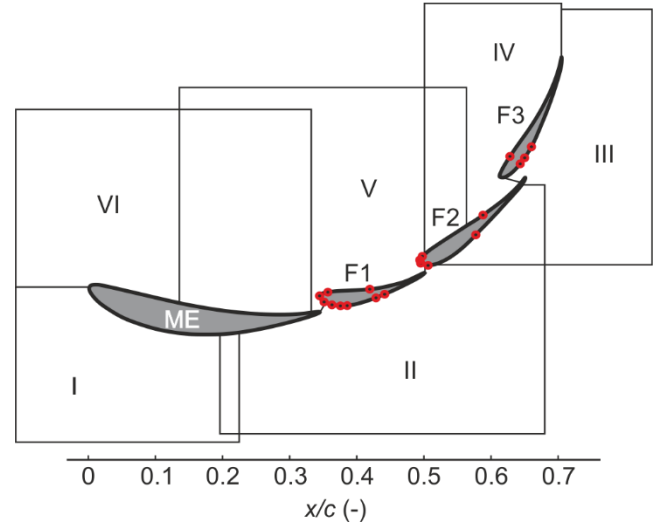


Figure 6. Locations of PIV measurement planes I to VI and pressure taps (marked by red circles).

# Results

In the following chapter, the results of the preliminary and main experimental investigation are presented. Focus will be laid upon the detection of the separated flow region and its influence on the aerodynamic performance of the rear wing in terms of the load acting on the three flaps. Then, the effect of the employed ASC approach on the flow field on the suction side of the upper flap and on the resulting aerodynamic load will be outlined.

## Assessment of Stand-Alone Rear Wing

This section includes results of the preliminary investigation of the stand-alone rear wing. Qualitative flow visualization as well as PIV and pressure measurements will be addressed.

### Onset and Influence of Flow Separation

To determine the increments in angle of attack of the upper flap $\Delta\alpha_{F3}$ that cause flow separation, UV active tufts were affixed to the suction side of the upper flap. Heavy fluctuations in the tuft orientations indicate highly turbulent or separated flow, see Figure 7.

The displayed long-exposure images show low tuft fluctuations at the design angle of attack ($\Delta\alpha_{F3} = 0°$), pointing to an attached flow on the upper wing element. The same is true for an increment of $\Delta\alpha_{F3} = 10°$. It is also interesting to note that tufts located near the symmetry plane are aligned with the flap chord whereas the outward directed velocity component appears to become more dominant with increasing distance to the plane of symmetry.

Increasing the upper element angle of attack by $\Delta\alpha_{F3} = 20°$ or $\Delta\alpha_{F3} = 25°$ results in distinct flattering of the applied tufts with the orientation of individual tufts indicating recirculating flow.
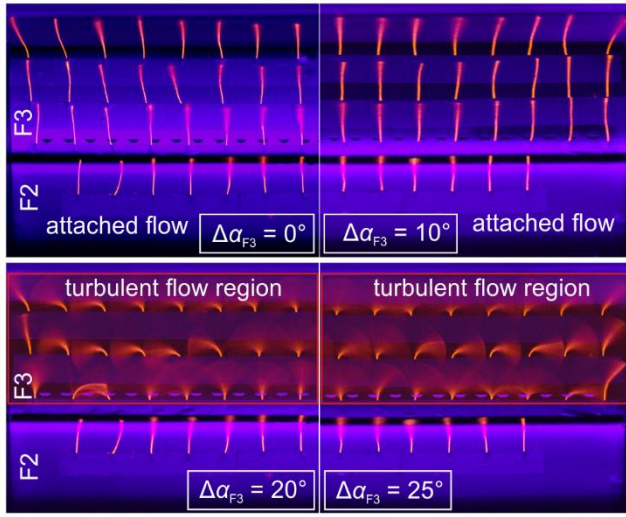
*Figure 7. Surface tuft visualization for investigated angle of attack increments (investigation of stand-alone rear wing).*

More detailed information regarding the flow field both on the suction and on the pressure side of the entire rear wing can be obtained from Figure 8 where the time-averaged velocity magnitude $U_{\mathrm{mag}} = \sqrt{u^2 + v^2 + w^2}$ is displayed for the non-actuated configuration under the angle of attack variation.
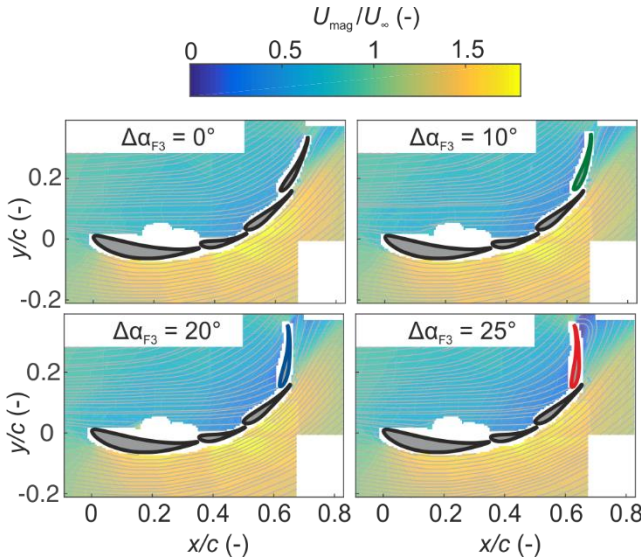


*Figure 8. Normalized velocity fields $U_{mag}/U_\infty = \sqrt{u^2 + v^2 + w^2}/U_\infty$ around rear wing subject to varied angle of attack of upper flap F3 (investigation of stand-alone rear wing); note that due to limited optical access (rear wing mounting), no data is available inside the white area on the main element pressure side .*

For all investigated angle of attack increments, a significant acceleration of the flow along the suction side of the rear wing compared to the free stream can be observed. A maximum in velocity magnitude of the order of $U_{\mathrm{mag}}/U_\infty \approx 1.8$ can be found to span the flaps F1 and F2. Therefore, a vast proportion of the generated downforce can be expected to be contributed by these wing elements.

As for the upper flap F3, a deficit in velocity magnitude is observed on the suction side for all angles of attack. However, the flow is still

attached at the design angle and for the smallest increment of $\Delta\alpha_{F3} = 10°$, agreeing well with the observations based on the tuft visualizations. In contrast, a small area of recirculating flow can be found on the trailing edge of F3 at $\Delta\alpha_{F3} = 20°$. The mean location of flow separation is then further shifted towards the leading edge at $\Delta\alpha_{F3} = 25°$, resulting in a sizable region of separated flow for this configuration.

The onset of flow separation has a distinct effect on the local velocity direction as the flow is directed increasingly vertical when the angle of attack of the upper element is raised. However, the separated flow can be associated with a blockage effect, yielding a more horizontal orientation of the shown time-averaged streamlines in this area. Furthermore, the flow separation on the upper flap appears to affect the flow field further upstream as well, as the maximum in velocity magnitude on the suction sides of F1 and F2 is slightly lower when compared to the configurations that exhibit an attached flow on the upper wing element. Therefore, a lower suction peak is expected when an angle of attack increment of $\Delta\alpha_{F3} = 25°$ is employed.

Whereas the implications of the found flow separation are generally negative in terms of the downforce that is generated by the suction side of the rear wing, the same is not true for the pressure side. Here, the velocity magnitude decreases when the angle of attack of F3 is raised. Thereby, kinetic energy is converted into pressure that is contributing favorably to the downforce generated by the rear wing.

The measured pressure distributions on the three flaps for the varied angle of attack of the upper element are shown in Figure 10. Generally, it can be noted that the magnitude of pressure on the pressure sides is similar for all flaps, corresponding to coefficients of the order of $c_p \approx 0.3$. On the suction side, a maximum in pressure magnitude yielding $c_p \approx -0.9$ is reached on F1 with pressure coefficients decreasing in magnitude further downstream.

When the angle of attack of the upper flap is increased, the magnitude of pressure is raised from $c_p \approx -0.4$ at $\Delta\alpha_{F3} = 0°$ to $c_p \approx -0.6$ at $\Delta\alpha_{F3} = 10°$ initially. However, for further increased angles of attack, the pressure coefficient drops in magnitude and reaches lower values than for the design angle of attack. This can be attributed to the occurrence of flow separation and agrees well with the previously discussed flow field data. It is also worth noting that the projected area that contributes to the overall downforce generated by flap F3 is smaller when greater angles of attack are employed. This can be expected to extent the performance drop when flow separation occurs on the upper flap.

The flow situation on the suction side of flap F3 also appears to affect the pressure distributions on the other flaps, as pressure coefficients initially increase at $\Delta\alpha_{F3} = 10°$ before a stagnation can be observed at $\Delta\alpha_{F3} = 20°$. For the greatest investigated angle of attack increment, the pressure magnitude decreases although it remains slightly greater than for the design angle of attack.

As opposed to the observations regarding the suction sides of the three flaps, the influence of the angle of attack variation is rather small on the pressure sides. However, it can be noted that the measured pressure coefficients increase consistently by small

margins when the angle of attack is raised. This effect is in accordance with the mentioned deceleration of fluid displayed in Figure 8.
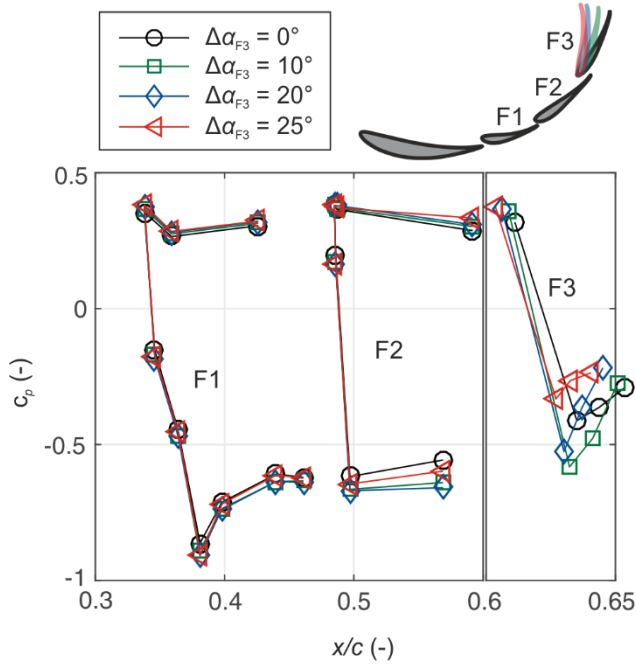


Figure 10. Pressure distribution on flaps subject to varied angle of attack of upper wing element F3 (investigation of stand-alone rear wing); abscissa adjusted for F3 for reasons of clarity.

**Control of Flow Separation**

In terms of the generated downforce, a negative influence can be expected when the upper element angle of attack is increased beyond a certain threshold that marks the onset of flow separation. In the present study, this appears to involve the increments $\Delta\alpha_{F3} = 20°$ and $\Delta\alpha_{F3} = 25°$ whereas an increase by $\Delta\alpha_{F3} = 10°$ may even result in an increased performance of the rear wing compared to the design angle of attack.

In order to suppress the observed flow separation, sweeping jets were emitted with a varying degree of actuation intensity. The influence of this approach on the mean vorticity field on the suction side of the upper flap is shown in Figure 9.

In this particular scenario, a region of great positive vorticity coincides with recirculating flow. Such an area can be found on the trailing edge of the flap for the non-actuated configuration and may be associated with a decreased performance as discussed previously. Actuation with a velocity ratio of $r = 1$ ($c_\mu = 0.04$ %) does not entirely suppress flow separation but significantly reduces the recirculation zone. As for the two greatest studied actuation intensities, no flow separation is visible. The area on the flap trailing edge is rather characterized by negative vorticity which indicates the attached fluid flowing off the suction side.

Both the direction and magnitude of the local flow velocity are affected by the applied ASC method as the area close to the suction side is characterized by more vertical flow when the separation is suppressed by the emission of sweeping jets. In addition, the velocity appears to be increased due to the greater momentum input.
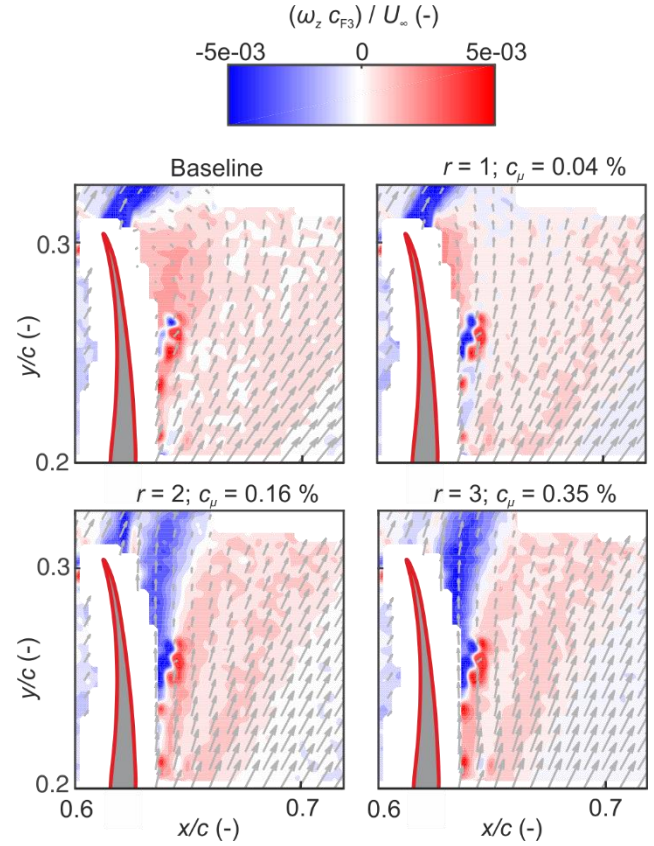
01/14/2019



Figure 9. Normalized vorticity on suction side of upper flap F3 subject to varied momentum input (investigation of stand-alone rear wing).

The influence of the pursued ASC method on the pressure distribution of the three flaps is exemplarily shown for an angle of attack increase by $\Delta\alpha_{F3} = 25°$ under variation of the momentum input in Figure 11.

As for the distributions on the pressure sides of the rear wing elements, there is no visible influence of the sweeping jets.

In contrast, the applied actuation consistently increases the pressure magnitude on the suction side. This is especially true for the upper flap F3 where the suction peak is significantly increased corresponding to a decrease of pressure coefficients from $c_p \approx -0.3$ (baseline) to $c_p \approx -0.75$ at the greatest actuation intensity. Similarly, an increasing pressure magnitude can be found on flap F2 where the level of pressure coefficients is decreased by roughly 20 %. Even on the lower flap F1, a positive influence can be noted so that generally, a better aerodynamic performance with respect to the generated downforce is to be expected when actuation is applied.
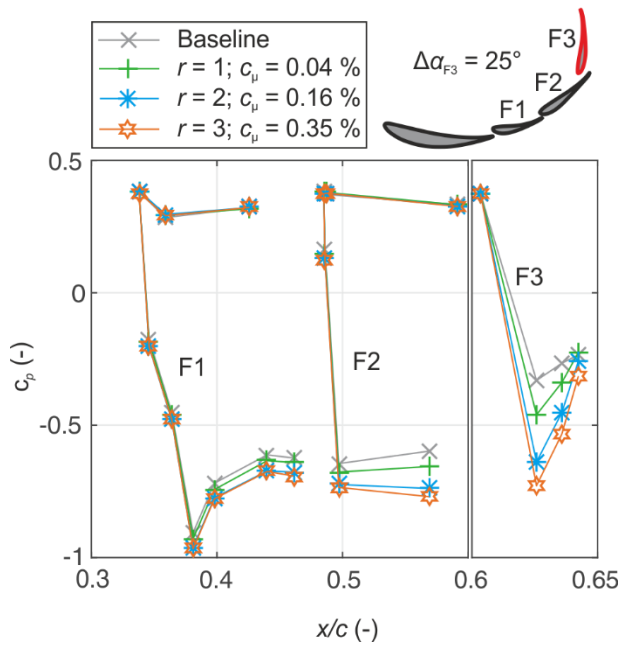
Figure 11. Pressure distribution on flaps subject to varied actuation intensity at an angle of attack of the upper flap F3 $\Delta\alpha_{F3} = 25°$ (investigation of stand-alone rear wing); abscissa adjusted for F3 for reasons of clarity.

## Aerodynamic Properties of Entire Race Car Model

The following section focuses on the main measurement campaign where the overall benefit of the chosen AFC approach for the entire race car was investigated. Again, PIV and pressure measurements are presented and compared to previously discussed results while also evaluating the aerodynamic load subject to varied angles of attack and momentum input.

### Influence of Increased Flap Angle of Attack

At first, the angle of attack of the upper flap was varied in the range of $\Delta\alpha_{F3} = [10, 20, 30, 40]°$ to determine the onset and impact of any occurring flow separation caused by the adverse pressure gradient on the suction side of the flap.

Generally, an attached flow can be noted for the smaller increments up to $\Delta\alpha_{F3} = 20°$ (Figure 12) that were already investigated in the preliminary experiment. However, the velocity magnitude close to the flap surface appears to be significantly greater when the entire vehicle is investigated. As a result, the kinetic energy in the boundary layer is greater and flow separation only sets in at the flap trailing edge at an angle increment of $\Delta\alpha_{F3} = 30°$. This deviation may be attributed to the altered mean direction of the incoming flow when the entire race car is considered in contrast to the horizontal free stream in the preliminary study. In particular, the negative angle of attack of the main wing element is designed to guide the slightly downward directed flow towards the rear wing flaps. However, for excessive angle of attack increments ($\Delta\alpha_{F3} \geq 30°$), flow separation does occur, culminating in a massively stalled flap for $\Delta\alpha_{F3} = 40°$, as shown in Figure 12.
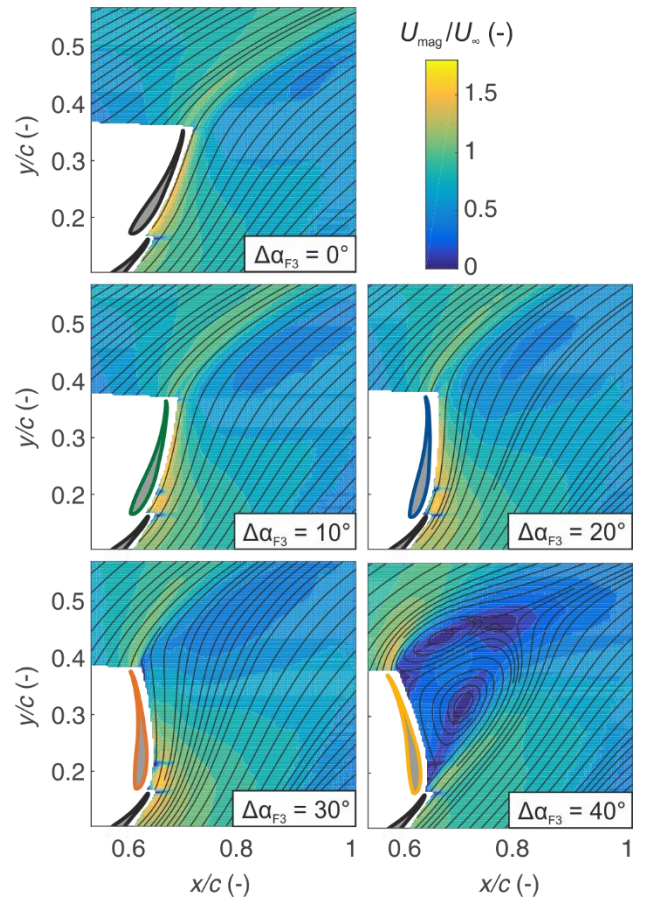


Figure 12. Normalized velocity magnitude on the suction side of the upper flap F3 subject to varied angle of attack (investigation of entire race car model).

The surface pressure distributions associated with the discussed velocity fields are shown in Figure 13. In accordance with the apparently better guided flow, the magnitude in pressure coefficients is distinctly greater than for the experiments of the separate rear wing (Figure 10). Whereas coefficients were previously ranging between $c_p \approx -0.9$ and $c_p \approx 0.4$, extrema in the case of the complete race car are of the order of $c_p \approx -1.7$ and $c_p \approx 0.7$ respectively.

As for the upper flap F3, there is a distinct increase in pressure magnitude when the moderate angle of attack increments $\Delta\alpha_{F3} = 10°$ and $\Delta\alpha_{F3} = 20°$ are considered. As flow separation sets in at greater angles, the suction intensity stagnates ($\Delta\alpha_{F3} = 30°$) before dropping distinctly from $c_p \approx -1.7$ to $c_p \approx -0.7$ when the upper flap is stalled at $\Delta\alpha_{F3} = 40°$. It should be noted that for the two greater angle of attack increments, a negative pressure on the suction side of the upper flap does not contribute towards the downforce but (positive) lift of the race car since the angle of attack of the upper flap is greater than 90° and surface normal vectors located at the pressure taps are pointing upwards. However, the pressure distribution on the upper flap must not be viewed separately since the majority of downforce is generated by the other wing elements with greater projection areas and these may feature more favorable pressure contributions when the upper flap is operated at greater angles of attack and actuation is applied.

In terms of the pressure distributions on the suction sides of the two lower flaps, an initial increase in magnitude is again apparent while

greater angles of attack are associated with slight decreases in pressure magnitude. On the pressure sides, however, these angles appear to cause a deceleration of fluid which is accompanied by increased pressure coefficients.
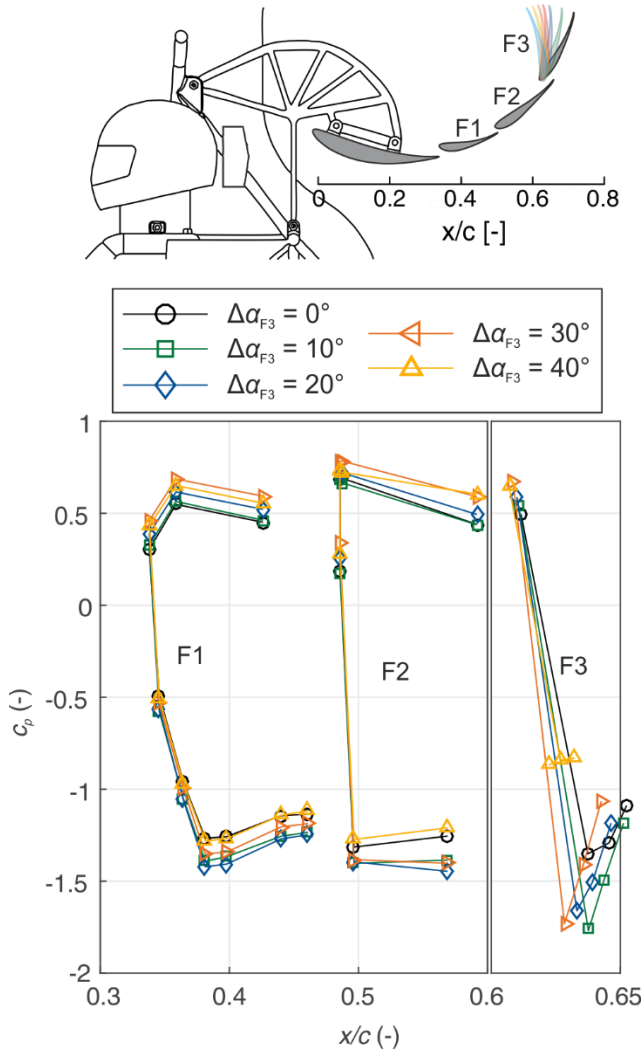


*Figure 13. Pressure distribution on rear wing flaps subject to varied angle of attack of upper flap F3 (investigation of entire race car model); abscissa adjusted for F3 for reasons of clarity.*

When analyzing the measured pressure distributions, it is worth pointing out that there is no data for the main wing element which has by far the greatest projection area contributing to the generated downforce. To capture the effects of the performed angle of attack variation on the entire race car, forces and moments acting on the model were measured. This allows for the calculation of aerodynamic coefficients addressed in the following.

The negative lift coefficient corresponding to the overall downforce at different angles of attack of flap F3 is depicted in Figure 14. Coefficients are shown for yaw angles of $\beta = -21 \ldots 21°$, representing relevant crosswind conditions.

Considering the passively optimized flap setup ($\Delta\alpha_{F3} = 0°$), maximum downforce corresponding to $-c_L \approx 1.58$ is achieved at zero-yaw condition. Compared to the employment of a three-element

rear wing investigated in [21], this represents an increase by $\Delta c_L \approx$ 5%. Under crosswind conditions, the downforce drops distinctly with a slight asymmetry apparent as smaller negative lift coefficients are found at negative yaw angles.

Increasing the upper element angle of attack results in a distinct enhancement for $\Delta\alpha_{F3} = 10°$ across all investigated yaw angles. This trend continues for the $\Delta\alpha_{F3} = 20°$ configuration which features increased lift coefficient up to $-c_L \approx 1.78$ for moderate yaw angles. A further increased angle of attack does not result in an increased maximum. However, the downforce performance is distinctly improved at yaw angles of $|\beta| > 10°$. Finally, the greatest investigated angle of attack is consistently associated with a performance drop when compared to the other configurations with raised angles of attack and features negative lift coefficients with a maximum of $-c_L \approx 1.6$.
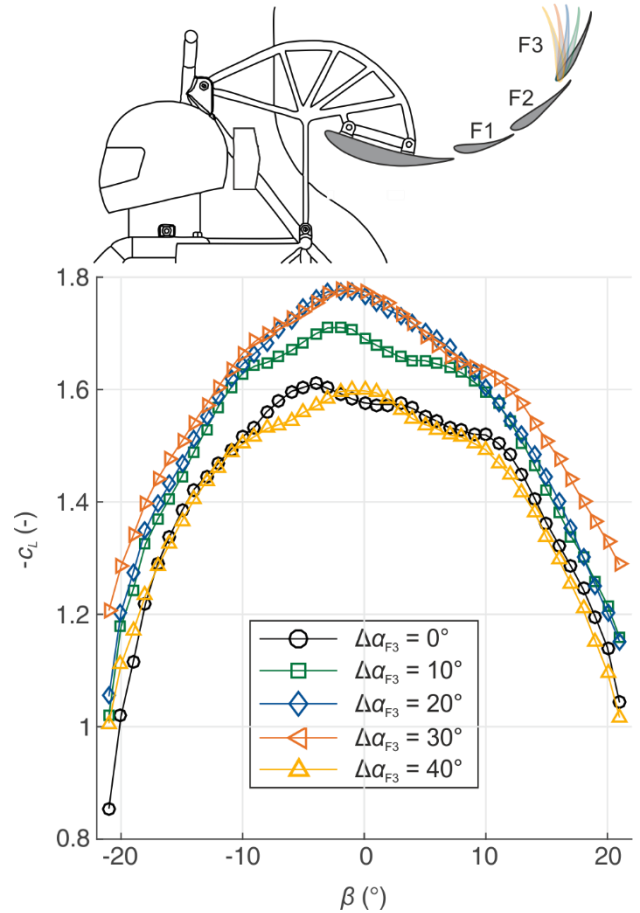


*Figure 14. Negative lift coefficient generated by entire race car subject to varied angle of attack of upper flap F3 and different yaw angles.*

The drag coefficients for the discussed configurations are shown in Figure 15. For a wide range of yaw angles $\beta = -18 \ldots 13°$, the baseline case ($\Delta\alpha_{F3} = 0°$) exhibits the smallest values with a maximum of $c_D \approx 1.2$. Again, this amounts to an increase compared to the previously employed rear wing that generates a maximum drag of $c_D \approx 1.05$.

When the angle of attack of the upper flap is raised, a gradual increase of the drag can be noted initially up to a coefficient of the order of $c_D \approx 1.38$ for $\Delta\alpha_{F3} = 30°$. Since the increments $\Delta\alpha_{F3} =$

01/14/2019

$20°$ and $\Delta\alpha_{F3} = 30°$ correspond to angles of attack $\alpha_{F3} = 83.3°$ and $\alpha_{F3} = 93.3°$, i.e., an almost vertically oriented flap, maximum drag can be expected for these configurations. Furthermore, the substitute chord length of the upper flap is increased due to the vertical direction of flow leaving the trailing edge, which also results in an increased drag. As for the greatest increment ($\Delta\alpha_{F3} = 40°$), pressure coefficients on the suction side of flap F3 drop distinctly as shown previously and additionally, the projection area of the upper flap contributing to the aerodynamic drag is again decreased. This results in a decreased maximum drag coefficient of $c_D \approx 1.26$.
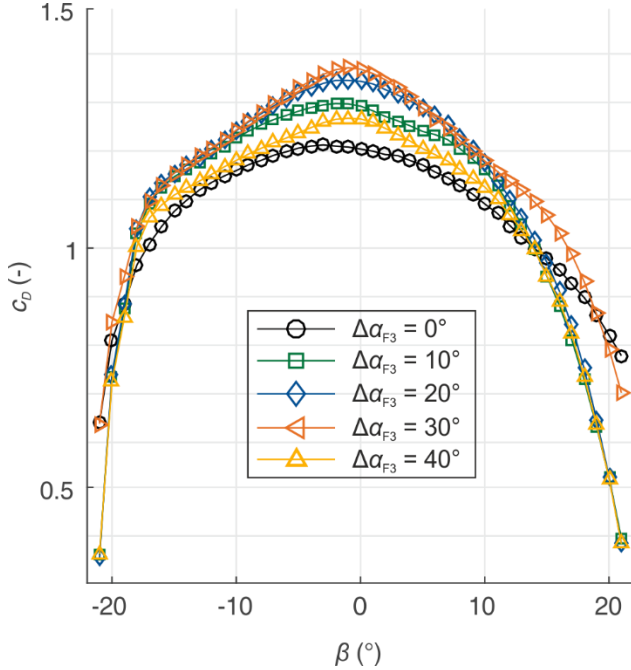


Figure 15. Drag coefficient generated by entire race car subject to varied angle of attack of upper flap F3 and different yaw angles.

## Influence of Active Separation Control

Whereas the previous findings discussed in this chapter referred to the race car model without ASC, we address the influence of this measure for distinctly increased angles of attack of the upper wing element in the following.

Figure 16 shows the mean velocity fields for $\Delta\alpha_{F3} = [30, 35, 40]°$ subject to different velocity ratios. For the smallest angle of attack, intermittent flow separation begins to occur at the flap trailing edge. When actuation is applied, the region of velocity deficit is eliminated and the velocity magnitude on the suction side of flap F3 is distinctly increased. For $\Delta\alpha_{F3} = 35°$, a large recirculation zone is apparent for the non-actuated scenario. This area is decreased through actuation at a velocity ratio of $r = 2$ and completely suppressed at $r = 5$, resulting in greater flow velocities on the suction side of the upper flap. As for the greatest studied increment of $\Delta\alpha_{F3} = 40°$, the region of separated flow is decreased in size as the centers of the two dominant vortices are shifted toward the flap, but no complete elimination is found for the greatest applied momentum input. However, a greater velocity magnitude can again be observed on the trailing edge of flap F2.
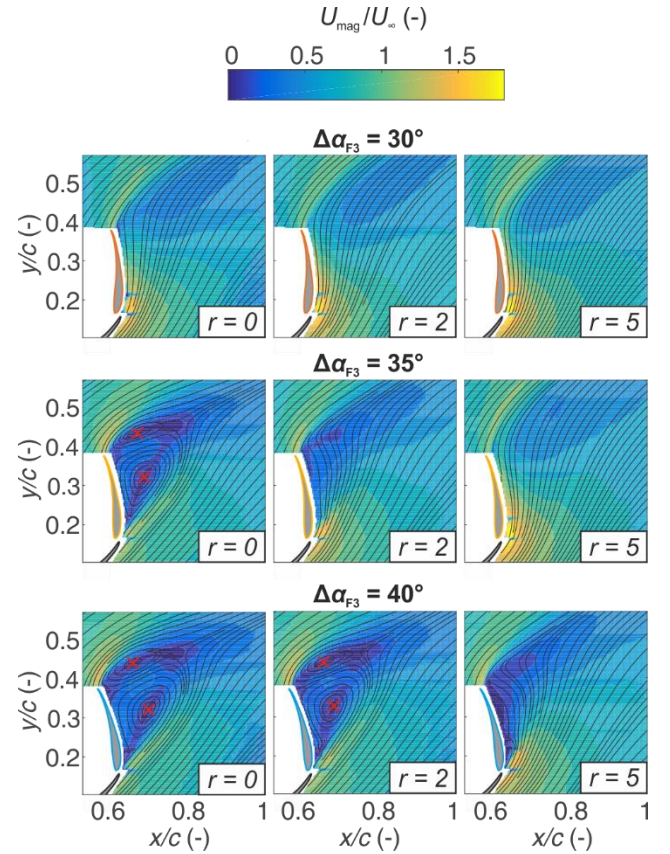


Figure 16. Normalized velocity magnitude on the suction side of the upper flap F3 at three different angles of attack subject to varied momentum input; vortex cores of recirculation zone marked by red cross (investigation of entire race car model).

The influence of a varied velocity ratio on the pressure distribution on the three flaps at $\Delta\alpha_{F3} = 40°$ is shown in Figure 17. Generally, there is a negligible effect on the pressure coefficients on the pressure sides as the flow field is apparently not affected by the ASC measure. On the suction side of the upper flap, however, the magnitude in pressure is distinctly increased from $c_p \approx -0.8$ (no ASC) to $c_p \approx -2.3$ ($r = 5$). The manipulated flow field on flap F3 also affects the pressure distributions on F1 and F2 as the suction intensity is consistently increased when the momentum input is raised.
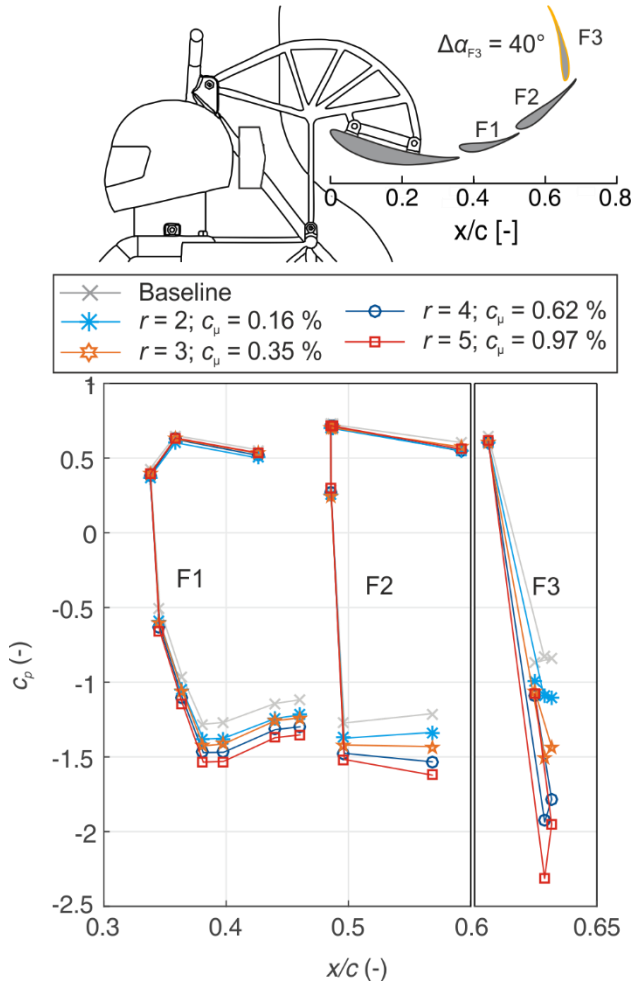
Figure 17. Pressure distribution on rear wing flaps subject to varied momentum input (investigation of entire race car model) ; abscissa adjusted for F3 for reasons of clarity.

characterized by an increased pressure magnitude on the suction side which distinctly contributes to the aerodynamic drag.
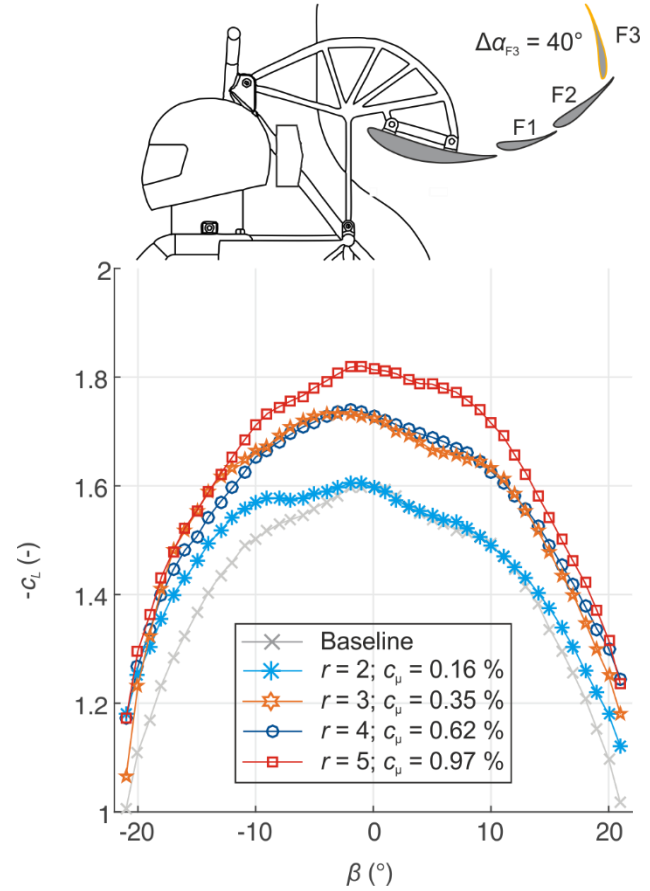


Figure 18. Negative lift coefficient generated by entire race car at $\Delta\alpha_{F3} = 40°$ subject to varied momentum input for different yaw angles.
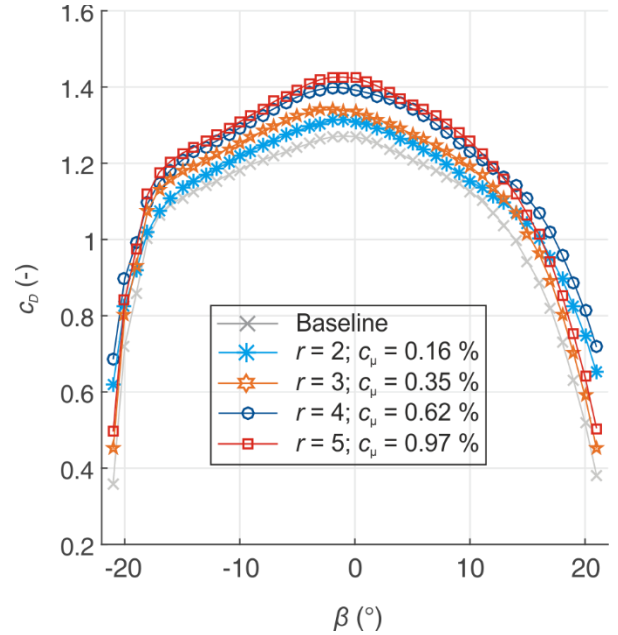
The corresponding negative lift coefficients are displayed in Figure 18. Both for the non-actuated case and for a small velocity ratio of $r = 2$, a maximum downforce corresponding to $-c_L \approx 1.6$ can be noted at $\beta = 0°$. For greater yaw angles, the actuated case is associated with greater downforce although a slight asymmetry can be observed as negative lift coefficients are consistently greater for negative yaw angles when actuation is employed. Increasing the momentum input results in systematically increased negative lift coefficients of $-c_L \approx 1.73$ at $r = 3$ and $r = 4$. Interestingly, there is almost no deviation between these configurations in terms of the generated downforce. This may be ascribed to the increased lift produced by the upper flap, which offsets the greater downforce induced by the other flaps.

The greatest momentum input again yields a significantly greater downforce with a maximum of $-c_L \approx 1.8$, representing an increase by $\Delta c_L \approx 11$ % compared to the non-actuated case.

However, the configuration yielding the greatest downforce is also associated with the largest drag coefficients as shown in Figure 19. Generally, there is a consistent increase in drag coefficients from $c_D \approx 1.27$ (no ASC) to $c_D \approx 1.42$ (greatest actuation intensity). This is in good agreement with the previously discussed pressure distributions. In particular, flap F3 that is almost vertically oriented is



Figure 19. Drag coefficient generated by entire race car at $\Delta\alpha_{F3} = 40°$ subject to varied momentum input for different yaw angles.

# Influence of Active Separation Control on Lap Times

From the results presented in the previous sections, it is apparent that distinct increases in the overall downforce are feasible by increasing the angle of attack of the upper flap coupled with local actuation. However, an enhanced negative lift appears to be invariably linked with greater drag coefficients. Therefore, the crucial question remains: is there a net benefit of the applied approach and if so, does it justify the increased design effort to implement the ASC system?

Based on an in-house lap time simulation that considers the vehicle mass, motor and tire characteristics, gearing as well as aerodynamic properties, the concrete influence of aerodynamic coefficients was established: whereas an increase in drag by $\Delta c_D = 1$ results in a lap time increase by 0.5 %, a margin of $\Delta(-c_L) = 1$ yields a lap time reduction of $\Delta t = 0.75$ % at the Formula Student Germany race circuit at Hockenheim.

Figure 20 shows the deviation in aerodynamic lift and drag for all studied configurations at $\beta = 0°$.

As for the baseline case, an initial increase in downforce can be observed when the flap angle of attack is increased. After a maximum corresponding to increments of $\Delta\alpha_{F3} = [20, 30]°$, a performance drop is observed for greater angles of attack due to flow separation. When actuation is applied, negative lift coefficients are greater for all investigated configurations and there is a clear trend indicating that greater downforce is generated at higher actuation intensities. The maximum downforce gain is achieved at an angle of attack increment of $\Delta\alpha_{F3} = 20°$ at the greatest momentum input, corresponding to an enhancement by roughly 22 % compared to the passively optimized flap setup. It is worth noting that the observed improvement in downforce performance is partly due to suppressed flow separation otherwise present at large angles of attack whereas for increments $\Delta\alpha_{F3} < 30°$, the positive effect of unsteady blowing can be attributed to an increased circulation.

Generally, increasing angles of attack of the upper flap and greater velocity ratios are associated by increased drag coefficients as displayed in the second diagram in Figure 20. This can be explained by the varied projection area of the flap (substitute) surface that reaches a maximum at $\Delta\alpha_{F3} = 30°$ corresponding to an angle of attack of $\alpha_{F3} = 93.3°$. Furthermore, the pressure distribution on the suction side of flap F3 is strongly dependent on the momentum input, exhibiting a significantly increased pressure magnitude when the actuation intensity is raised.

Based on the discussed deviations in downforce and drag, the potential for lap time reductions was deduced (third diagram in Figure 20). Interestingly, all investigated configurations lead to a lap time reduction when compared to the non-actuated baseline setup. However, actuation appears to only yield a considerable benefit for the two greatest velocity ratios ($r = 4$ and $r = 5$) whereas the net benefit is marginal otherwise. Based on the studied angle of attack increments, $\Delta\alpha_{F3} = 20°$ appears to be the most beneficial scenario, resulting in a significant lap time reduction of $\Delta t = 0.17$ % translating to roughly 0.15 seconds per lap at the Hockenheim circuit. This is mainly due to a smaller drag coefficient compared to $\Delta\alpha_{F3} = 30°$ which is associated with a downforce of roughly the same order of magnitude.
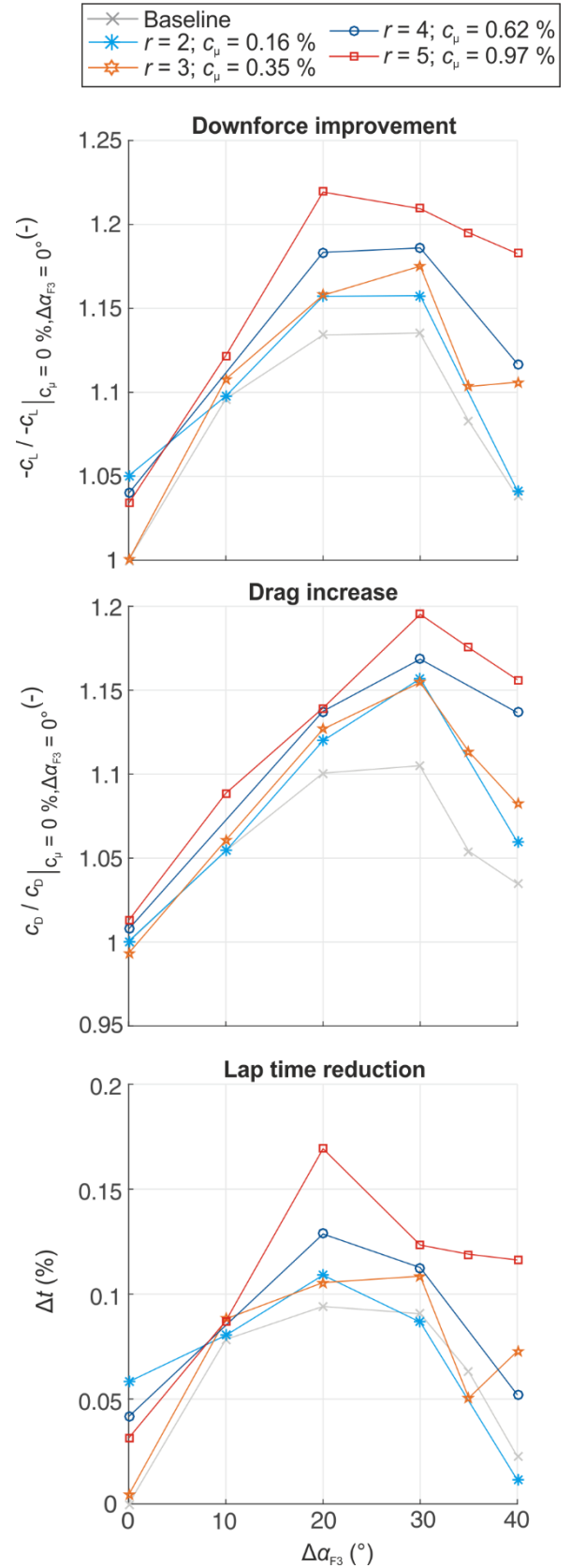


*Figure 20. Influence of actuation intensity and upper flap angle of attack on downforce, drag and lap time reduction.*

01/14/2019

Finally, it should be noted that the computation of lap time reductions utilized here is designed for an endurance race and permanent actuation. However, there are competitions, such as skidpad or acceleration races, that benefit from increased downforces to a much greater extent while increased drag coefficients are almost negligible.

## Conclusions and Outlook

Generally, the present article demonstrates the potential of fluidic actuators to enhance the aerodynamic properties of race cars with multi-element wing configurations. While similar investigations have been successfully conducted in the field of high-lift aerodynamics, we are not aware of ASC applications on race cars even though the desire to achieve performance gains might be just as great.

Furthermore, it was shown that an individual assessment of the rear wing is justified to prove the general capability of ASC devices. However, the analysis regarding the complete race car is essential as critical angles of attack heavily deviate between both test setups.

To improve the aerodynamic performance of the investigated race car, re-designing the wing elements may be recommended as the current setup is passively optimized and does not take actuation by means of fluidic devise into account.

The following step consists in the validation of the approach through road testing. Along with issues of the technical implementation, it needs to be ensured that the safe drivability of the race car is still ensured if the ASC system fails. Based on measurements of the pitching moment, the downforce acting on the rear axle is decreased by 3 % when the entire array of fluidic devices is suddenly switched off at the identified optimum parameter combination ($\Delta\alpha_{F3} = 30°$, $r = 5$). Another potential scenario involves the failure of half of the actuators as they are currently supplied by two separate tubes, resulting in a potentially critical roll moment. However, looking at this the other way around, a more sophisticated application of the ASC system would enable better control of the car. For instance, an application only in corners would marginalize the drag penalty that particularly affects the driving speed in straight sections. Furthermore, a partial application of the devices would possibly allow for faster cornering as the yaw and roll moments are more favorable.

The other remaining issue consists in finding a solution for the necessary mass flow supply. According to the in-house lap time simulation, it can be concluded that the identified performance enhancement due to the studied ASC method equals a mass reduction of the race car by roughly 3.0 kg. On that basis, three potential implementation strategies can be drafted. First, a small-scale compressor can be installed in the race car with the additional mass of this device, the fluidic actuators and required tubing not exceeding 3.0 kg. Alternatively, the mass flow consumption can be covered by exhaust gas but then, the material of tubing and fluidic devices must be carefully chosen as to withstand high thermal loads. Third, a small gas cylinder may be placed in the vehicle to feed the ASC devices. While the gas volume might not be sufficient for endurance races, the required mass flow for acceleration and skidpad races can be easily met.

## References

1. Dominy, R. G., "Aerodynamics of Grand Prix Cars," *Proc. Instn. Mech. Engrs.* 206(44):267-274, 1992, doi: 10.1243/PIME_PROC_1992_206_187_02.
2. Jasinski, W. J. and Selig, M. S., "Experimental Study of Open-Wheel Race-Car Front Wings," SAE Technical Paper 983042, 1998, doi: 10.4271/983042.
3. Katz, J., "Aerodynamics of Race Cars," *Annu. Rev. Fluid Mech.* 38:27-63, 2006, doi: 10.1146/annurev.fluid.38.050304.092016.
4. Greenblatt, D. and Wygnanski, I. J. "The Control of Flow Separation by Periodic Excitation," *Prog. Aerosp. Sci.* 36(7):487-545, 2000, doi: 10.1016/S0376-0421(00)00008-7.
5. Seifert, A., Greenblatt, D. and Wygnanski, I. J. „Active Separation Control: An Overview of Reynolds and Mach Numbers Effects," *Aerosp. Sci Techn.* 8(7):569-582, 2004, doi: 10.1016/j.ast.2004.06.007.
6. Steinfurth, B. and Haucke, F. "Coherent Structures in the Actively Controlled Wake of a High-Lift Configuration," *AIAA J.* 56(10):3848-3856, doi: 10.2514/1.J057094.
7. Glezer, A. and Amitay, M. „Synthetic Jets," *Annu. Rev. Fluid Mech.* 34:503-529, 2002, doi: 10.1146/annurev.fluid.34.090501.094913.
8. Corke, T. C., Enloe, C. L. and Wilkinson, S. P. "Dielectric Barrier Discharge Plasma Actuators for Flow Control," *Annu. Rev. Fluid Mech.* 42:505-529, doi: 10.1146/annurev-fluid-121108-145550.
9. Bauer, M., Grund, T., Nitsche, W. "Experiments on Active Drag Reduction on a Complex Outer Wing Model," *AIAA J.* 53(7):1774-1783, 2015, doi: 10.2514/1.J053515.
10. Raghu, S. "Fluidic Oscillators for Flow Control," *Exp. Fluids* 54(1), 2013, doi: 10.1007/s00348-012-1455-5.
11. Seo, J. H., Zhu, C. and Mittal, R. "Flow Physics and Frequency Scaling of Sweeping Jet Fluidic Oscillators," *AIAA J.* 56(6), 2018, doi: 10.2514/1.J056563.
12. Ostermann, F., Woszidlo, R., Nayeri, C. N. and Paschereit, C. O. „The Time-Resolved Flow Field of a Jet Emitted by a Fluidic oscillator into a Crossflow," *54th AIAA Aerospace Science Meeting*, AIAA 2016-0345, 2016, doi: 10.2514/6.2016-0345.
13. Seele, R., Graff, E. Gharib, M., Taubert, L., Lin, J. and Wygnanski, I. J. "Improving Rudder Effectiveness With Sweeping Jet Actuators," *6th AIAA Flow Control Conference*, 2012, doi: 10.2514/6.2012-3244.
14. Andino, M. Y., Lin, J. C., Washburn, A. E., Whalen, E. A., Graff, E. C. and Wygnanski, I. J. "Flow Separation Control on a Full-Scale Vertical Tail Model Using Sweeping Jet Actuators," *53rd AIAA Aerospace Sciences Meeting*, AIAA 2015-0785, 2015, doi: 10.2514/6.2015-0785.
15. Pack Melton, L. G., Koklu, M., Andino, M., Lin, J. C., Edelman, L. M. "Sweeping Jet Optimization Studies," *8th AIAA Flow Control Conference*, 2016, doi: 10.2514/6.2016-4233.
16. Wieser, D., Lang, H., Nayeri, C. N., Paschereit, C. O. „Manipulation of the Aerodynamic Behavior of the DrivAer Model with Fluidic Oscillators," *SAE Int. J. Passeng. Cars – Mech. Syst.* 8(2):687-702, 2015, doi: 10.4271/2015-01-1540.
17. Schmidt, H. J., Woszidlo, R., Nayeri, C. N., Paschereit, C. O. „Drag Reduction with Fluidic Oscillators on a Rectangular Bluff Body Equipped with Base Flaps," *Exp. Fluids* 56(7), 2015, doi: 10.1007/s00348-015-2018-3.
18. Metka, M., Gregory, J., Sassoon, A. and McKillen, J. "Scaling Considerations for Fluidic Oscillator Flow Control on the Square-Back Ahmed Vehicle Model," *SAE Int. J. Passeng. Cars – Mech. Syst.* 8(1):328-337, 2015, doi: 10.4271/2015-01-1561.

01/14/2019

19. Woszidlo, R. and Wygnanski, I. J. "Parameters Governing Separation Control with Sweeping Jet Actuators," *29th AIAA Applied Aerodynamics Conference*, 2011, doi: 10.2514/6.2011-3172.
20. Koklu, M. "Effects of Sweeping Jet Actuator Parameters on Flow Separation Control," *AIAA J.* 56(1):100-110, 2018, doi: 10.2514/1.J055796.
21. Steinfurth, B., Feldhus, S., Berthold, A. and Haucke, F. "Aerodynamic Behavior of Formula Student Open-Wheel Race Car Model with Regard to head Restraint7Rear Wing Interaction," SAE Technical Paper 2018-01-0724, 2018, doi: 10.4271/2018-01-0724.
22. Woszidlo, R., Ostermann, F., Nayeri, C. N., Paschereit, C. O. „The Time-Resolved Natural Flow Field of a Fluidic Oscillator," Exp. Fluids 56(6), 2015, doi: 10.1007/s00348-015-1993-8.
23. Hucho, W.-H. (ed.)., "Aerodynamik des Automobils," Springer Vieweg, 6th edition, 2013, doi: 10.1007/978-3-8348-2316-8.

## Definitions/Abbreviations

| | |
|---|---|
| **ASC** | Active separation control |
| **SJA** | Sweeping jet actuator |
| **ME** | Main element of rear wing |
| **F1** | Lower flap of rear wing |
| **F2** | Middle flap of rear wing |
| **F3** | Upper flap of rear wing |
| **UV** | ultraviolet |

01/14/2019

## Appendix



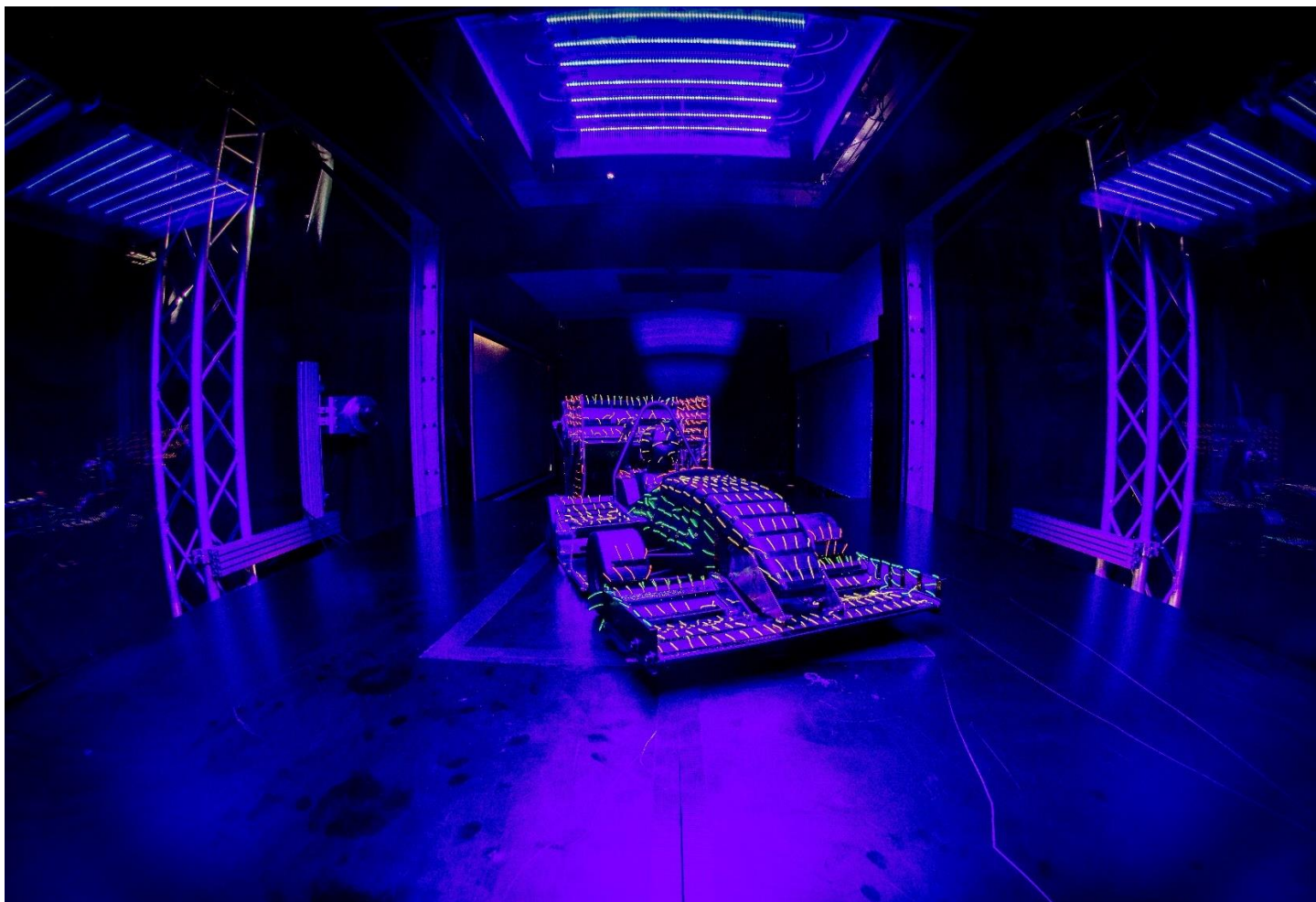*Figure A1. Investigated race car model inside wind tunnel test section at $\beta = 10°$.*

01/14/2019